Research Square

Preprints are preliminary reports that have not undergone peer review.
They should not be considered conclusive, used to inform clinical practice,
or referenced by the media as validated information.

High-efficiency antimony biomineralization by Serratia marcescens: process optimization and integrated genomic–transcriptomic–proteomic analysis

Zhiwei Zhou
Guizhou University
Peng Zhang
Guizhou University
Qing Li
Guizhou University
Huan Hu
Guizhou University
Xia Hu
Guizhou University
Aijiang Yang
yangaij8818@sina.com
Guizhou University

Research Article

Keywords: Antimony pollution, Microbial mineralization, Whole genome sequencing, Transcriptomics, Environmental remediation

Posted Date: August 24th, 2026

DOI: https://doi.org/10.21203/rs.3.rs-10650458/v1

License: This work is licensed under a Creative Commons Attribution 4.0 International License.
Read Full License

Additional Declarations: No competing interests reported.

High-efficiency antimony biomineralization by *Serratia marcescens:* process optimization and integrated genomic–transcriptomic–proteomic analysis

Zhiwei Zhou [a c], Peng Zhang [a, b c], Qing Li [a c], Huan Hu[a, c], Xia Hu [a, b, c], Aijiang Yang [a, b, c] *

[a] College of Resources and Environmental Engineering, Guizhou University, Guiyang 550025, PR China

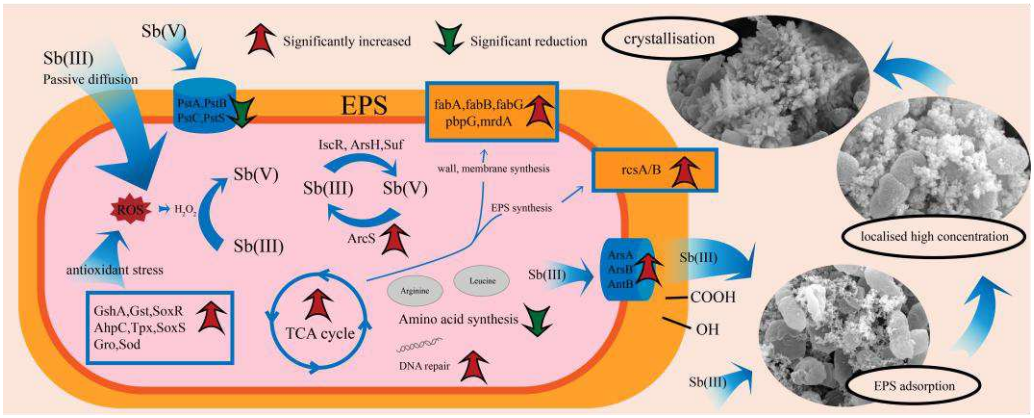
[b] Guizhou Karst Environmental Ecosystems Observation and Research Station, Ministry of Education, Guiyang 550025, PR China

[c] Institute of Environmental Engineering Planning and Designing, Guizhou University, Guiyang 550025, PR China

* To whom correspondence should be addressed

E-mail: yangaij8818@sina.com

Graphical abstract



ABSTRACT

This study aimed to isolate a novel antimony-mineralizing bacterium and elucidate its molecular response mechanisms during Sb(III) biomineralization via integrated multi-omics.

The isolate *Serratia marcescens* (MIC > 250 mM) achieved 96.18% Sb(III) removal under Box-Behnken-optimized conditions (27.7 ℃, pH 4.67, 205.6 rpm). Time-series Raman and SEM-EDS revealed a non-classical crystallization pathway proceeding through an amorphous precursor to crystalline Sb_2O_3 (confirmed by XRD/XPS) within 36 h. Integrated transcriptomic and proteomic profiling showed that Sb(III) stress significantly upregulated TCA cycle enzymes (*mqo*, *mdh*, *fumC*), fatty acid β-oxidation (*FadL/D/E/A*), siderophore/iron uptake (*entB/C/E*, *fepB/A*), Fe-S cluster assembly (*sufABCS*), molybdenum cofactor biosynthesis (*moaABCDE*), and glutathione-mediated antioxidant systems (*katCEG*, *gshAB*), while concurrently downregulating flagellar assembly (*flgBCDEFGKL*) and chemotaxis (*cheR*) to conserve proton motive force for *ArsB*-driven Sb(III) efflux.

S. marcescens orchestrates a coordinated metabolic reprogramming that enhances energy generation, metal sequestration, and oxidative defence while suppressing motility, effectively transforming toxic aqueous Sb(III) into valuable crystalline Sb_2O_3. These findings provide a mechanistic blueprint for engineering microbial-based bioremediation and resource recovery from antimony-polluted environments.

Keywords: Antimony pollution; Microbial mineralization; Whole genome sequencing; Transcriptomics; Environmental remediation

Impact Statement

Antimony contamination of water resources poses a global health risk, yet conventional remediation is costly and environmentally burdensome. This study demonstrates that *Serratia marcescens* efficiently biomineralizes Sb(III) into Sb_2O_3 crystals, and its multi-omics characterization reveals a coordinated metabolic reprogramming that couples energy conservation with metal detoxification. These insights establish a mechanistic basis for developing bio-engineered systems that recover critical metals from polluted environments, advancing a circular economy approach to environmental remediation.

1. Introduction

Antimony (Sb) is a toxic metalloid prevalent in terrestrial ecosystems.[1-3] Excessive Sb exposure can lead to organ failure, respiratory diseases, and may be carcinogenic.[4] Due to rapid urbanization and industrialization, Sb concentrations in water and soil have risen significantly.[5, 6] Sb is listed as a priority pollutant by both the U.S. Environmental Protection Agency (EPA) and the European Union (EU) Council.[4] Global Sb reserves are estimated at 1.8 million tons, with China (54%), Russia (18%), and Tajikistan (15%) accounting for 87% of world production.[7] As of 2021, China remained the leading global Sb producer, contributing 55% of mined output.[8] Stibnite (Sb_2S_3), the predominant Sb ore,[9] undergoes oxidation and leaching driven by oxygen, microbes, and water, generating acidic wastewater rich in Sb and sulfate, which contaminates surrounding environments.[10] For instance, surface water Sb concentrations near the Xikuangshan mining area in Hunan surged from 0.03 mg/L in pristine areas to 2.09 mg/L post-mining, far exceeding the drinking water Sb concentration limit (20 μg/L) set by the World Health Organization (2017).

Sb primarily exists in the -III, 0, III, and V oxidation states, with Sb(III) and Sb(V) being the most common environmental forms.[1] Toxicity depends on chemical form and oxidation state, generally following the order: elemental Sb > inorganic Sb salts > organic Sb species, and Sb(III) > Sb(V).[11] The main valence states of Sb in the environment are Sb(III) and Sb(V).[3] Microorganisms play crucial roles in Sb geochemical cycling, reducing its toxicity through bioreduction, biooxidation, and speciation changes,[12] thereby facilitating Sb complexation, mineralization, and biotransformation.[13] Microbial biomineralization of Sb, observed across diverse taxa, serves as a key tolerance mechanism within this biogeochemical cycle.[14] Lai et al.[15] reported autotrophic bacteria using hydrogen (H_2) as an electron donor to reduce Sb(V) to Sb_2O_3 in flooded mine soils. Yamamura et al.[16] identified the autotroph Geobacter sp. SVR, which transforms Sb(V) into Sb_2O_3, forming senarmontite or valentinite depending on pH. The fungus *Rhodotorula mucilaginosa* converts Sb(III) to less soluble crystalline Sb_2O_3 via extracellular polymeric substances (EPS).[17] Sulfate-reducing bacteria (SRB) contribute to Sb mineralization by adsorbing antimonate/antimonite onto cell surfaces and precipitating Sb_2S_3 or Sb_2S_5, often co-precipitating with phosphorus-containing groups.[18] Although significant progress has been made in understanding microbial Sb(III) or Sb(V) biomineralization, the vast diversity and functional heterogeneity of bacteria necessitates further mechanistic studies, the discovery of novel functional strains, and deeper insights into their roles in Sb biogeochemical cycling. Such knowledge is essential for elucidating the mechanisms of microbial Sb biomineralization and developing bioremediation technologies.

Nevertheless, the molecular and physiological mechanisms underlying microbially driven mineralization of aqueous Sb(III) into crystalline Sb_2O_3 remain largely unclear. A thorough elucidation of this pathway is essential for advancing our fundamental understanding of microbial contributions to antimony biogeochemistry and the formation of Sb_2O_3 biominerals. In this study, we aimed to systematically uncover the bacterial mechanisms responsible for the conversion of dissolved Sb(III) into crystalline Sb_2O_3 using an integrated multi-level approach. The specific objectives were to: (1) identify the optimal conditions for Sb(III) mineralization and clarify the influence of

environmental variables on this process; (2) characterize the evolution of mineral phases and changes in antimony coordination during biomineralization through multi-technique structural analysis; and (3) dissect the underlying regulatory network and functional pathways via integrated genomic, transcriptomic, and proteomic mining.

2. Materials and Methods

2.1. Strain source

In January 2024, c omposite samples were collected from the outlet of the Banpo Dongfeng Sb mine. The samples were kept at 4℃ and processed within 24 h. A chemically defined medium (CDM) was prepared for bacterial enrichment.[19] All reagents were of analytical grade.

The enriched bacterial culture was inoculated into CDM supplemented with 2% (w/v) agar to isolate single colonies based on morphological characteristics. Individual colonies were then transferred to CDM containing potassium antimony tartrate ($C_8H_4K_2O_{12}Sb_2 \cdot 3H_2O$, analytical reagent) as the Sb(III) source to enrich for Sb-tolerant strains. The Sb(III) concentration was progressively increased in each enrichment cycle to select bacteria capable of transforming antimony.

2.2. Sb(III) tolerance assay

To assess Sb(III) resistance, a chemically defined medium (CDM) was prepared with varying Sb(III) concentrations (0, 10, 50, 100, 150, 200, 250 mM; pH 7.2), along with uninoculated controls. The purified bacterial isolate was inoculated (1%, v/v) into 100 mL of CDM and incubated at 28 ℃ with shaking at 150 rpm. Optical density at 600 nm (OD_{600})[20] was measured at 4, 8, 12, 16, 20, and 24 h using a T6 UV-Vis spectrophotometer (Beijing General Instrument Co., China).[14] The minimum inhibitory concentration (MIC) was determined based on the OD_{600} measurements. All experiments were performed in triplicate.

2.3. Sb removal validation

Strains were cultured in CDM at 28 ℃ and 150 rpm with either 0 mM or 8.15 mM Sb(III) to observe precipitate formation. The precipitate-forming bacteria were then

inoculated (1%, v/v) into CDM containing initial Sb(III) concentrations of 0.41, 0.82, 4.1, or 8.2 mM and incubated for 5 days. Total Sb concentrations in the medium before and after incubation were determined by atomic fluorescence spectrometry (AFS).[21]

2.4. Response surface analysis

Single-factor experiments were conducted to investigate the effects of temperature (15, 25, 30 ℃), initial pH (4.0, 6.0, 7.0, 8.0), initial concentration of Sb(III) (8.14, 16.9, 24.43 mM; initial values, unadjusted), and shaking speed (100, 150, 200 rpm). The level for each factor corresponding to maximum Sb removal in the single-factor experiments were used to design a Box-Behnken design in Design-Expert 13, aiming to optimize the four factors for Sb(III) removal efficiency. Sb concentrations were measured by AFS.

2.5. Mineralized product characterization

The bacteria were cultured under the optimal mineralization conditions determined by response surface analysis. Precipitates were collected at 9, 12, 15, 18, 21, 24, 27, 30, 33, and 36 h, washed with sterile water, and then subjected to Raman spectroscopy. Raman spectra were collected using a WITec alpha300R spectrometer (Wealtec) at room temperature with 532 nm laser excitation. To minimize possible photo-induced changes, the laser power was limited using optical density filters and did not exceed 3 mW.

The precipitate obtained after 36 h was washed with sterile water, centrifuged (4 °C, 12,000 × g, 5 min), dried, and collected. X-ray photoelectron spectroscopy (XPS) and X-ray diffraction (XRD) measurements were performed by Hangzhou Yanqu Information Technology Co., Ltd.

2.6. Whole-genome and transcriptome sequencing analysis

For genomic analysis, purified S. marcescens colonies were harvested and subjected to Illumina (short-read) and PacBio (long-read) sequencing. Hybrid assembly was performed using Unicycler, and the complete genome was annotated with Prodigal, tRNAscan-SE, and Barrnap. Functional annotation was achieved using BLAST against the GO, KEGG, and COG databases. Strain identification was confirmed via 16S rRNA sequencing and phylogenetic analysis using MEGA 6.0.[22] For transcriptomic analysis,

cells grown under control conditions and Sb(III) stress (19.47 mM) were harvested at the logarithmic phase. Total RNA was extracted, rRNA-depleted, and sequenced on the Illumina NovaSeq 6000 platform. Clean reads were aligned to the reference genome using Bowtie2, and gene expression was quantified with RSEM. Differentially expressed genes ($|\log_2$ fold change$| \geq 1$, adjusted p-value < 0.05) were identified using DESeq2 and then subjected to GO and KEGG enrichment analyses.[23]

2.7. Proteomic analysis

Cells from the control and Sb(III)-treated groups were harvested at the logarithmic phase. Proteins were extracted using lysis buffer (8 M urea, 1% SDS) supplemented with protease inhibitors. After reduction, alkylation, and trypsin digestion, the resulting peptides were analyzed by LC-MS/MS on an Orbitrap Astral mass spectrometer operated in data-independent acquisition (DIA) mode. Raw data were processed with Spectronaut 19 for protein identification and quantification. Differentially expressed proteins ($|\log_2$ fold change$| \geq 0.263$, $p < 0.05$) were subjected to GO, KEGG, and protein-protein interaction (PPI) network analyses using DAVID, STRING, and Cytoscape (version 3.10.3).[24]

2.8. PPI network construction and data mining

Protein-protein interaction (PPI) network analysis of the annotated genes was performed using the STRING database (Search Tool for the Retrieval of Interacting Genes). Data sources were set to text mining, experiments, and databases. For the transcriptome-based PPI network, a minimum interaction score of 0.900 was used; for the proteome-based PPI network, a minimum score of 0.4 was applied. Key sub-network (cluster) analysis was carried out using the MCODE plugin in Cytoscape.

3. Results

3.1. Verification of Bacterial Functional Characteristics and Optimization of Efficiency

A Gram-negative bacterium forming smooth, bright red colonies was isolated and identified as *Serratia marcescens* via 16S rRNA sequencing. When cultured in chemically defined medium (CDM) containing 8.15 mM Sb(III), the strain induced visible

precipitate formation, whereas no precipitate was observed in Sb(III)-free medium, indicating its ability to transform aqueous Sb(III) into insoluble products. Atomic fluorescence spectrometry (AFS) quantification confirmed significant antimony removal, with removal efficiency increasing at higher initial Sb(III) concentrations (Figure 1a). The strain exhibited exceptional Sb(III) tolerance, with a minimum inhibitory concentration (MIC) exceeding 250 mM (Figure 1b).

Single-factor experiments showed that a temperature of 30 ℃, pH 4.0, Sb(III) concentration of 24.6 mM, and shaking speed of 200 rpm each enhanced Sb(III) removal (Appendix Figure S2). Subsequent Box-Behnken response surface methodology (RSM) optimization identified pH as the most influential factor (Appendix Figure S3). Variance analysis of the response surface model reveals a significant model regression and an insignificant lack-of-fit, which collectively substantiate the model's high predictive fidelity and justify its applicability in subsequent design exploration (Appendix Table S1). The optimal conditions were predicted to be 27.7 ℃, pH 4.67, shaking speed of 25.6 rpm, and an initial Sb(III) concentration of 19.47 mM, yielding a predicted removal rate of 97.3%. Validation experiments achieved 96.18% removal after 5 days, demonstrating high consistency with the model and confirming the robustness of the optimized conditions (Appendix Figure S4).

3.2 Phase structure and elemental composition of precipitate

To determine the composition of the precipitates generated under *Serratia marcescens* mediation, the obtained precipitates were processed and characterized by XRD and XPS; the results are shown in Figure 2a. Figure 2a shows the XRD pattern. The diffraction peaks of the mineralization product closely matched the reference pattern for Sb_2O_3 (PDF#05-0534), indicating that its crystalline phase is consistent with that of Sb_2O_3. Sharp diffraction peaks indicate that the sample is highly crystalline,[25] and no additional Sb-containing impurity peaks were detected. Figures 2b, 2c and 2d show the full scan XPS, C 1s and Sb 3d spectra, respectively. The full scan results indicate that the precipitate surface mainly contains Sb (antimony), O (oxygen) and C (carbon), and no other metal or impurity elements (e.g., Cl, S, etc.) were detected, which is consistent with the XRD results. The binding energy peak located at 284.8 eV was attributed to

C-C and this peak was used for binding energy calibration;[26] the binding energy peaks located at 286.32 eV and 287.95 eV may correspond to hydroxyl/ether bonds (C-OH/C-O-C) and carbonyl/carboxylic acid groups (C=O/O-C=O), respectively.[27] In the fine scan of Sb 3d, Sb $3d_{3/2}$ was used as the basis for peak splitting because the O 1s peak overlaps with that of Sb $3d_{5/2}$.[28] The binding energies of Sb $3d_{3/2}$ and Sb $3d_{5/2}$ were 539.08 eV and 529.68 eV, respectively, with a 9.4 eV peak spacing, which is consistent with the chemical state of Sb(III);[28] the spectral peaks of O 1s are located at 529.98 eV and 531.68 eV, respectively, where 529.98 eV is attributed to lattice oxygen (O^{2-}), corresponding to the metal-oxygen bonding in Sb_2O_3 (Sb-O),[28, 29] and 531.68 eV to surface adsorbed oxygen (e.g. hydroxy-OH or adsorbed water).[30, 31] Taken together, the mineralization product produced under *Serratia marcescens* mediation is identified as Sb_2O_3.

Raman spectra were collected over time (Figure 2e). Characteristic peaks for Sb_2O_3 began to appear at 27 h, with their intensity increasing thereafter. No Raman signals corresponding to antimony species were detected in samples collected prior to 27 h.

Figures 2f-h show scanning electron microscopy with energy dispersive spectroscopy (SEM-EDS) images of bacterial cultures at 12, 24, and 36 hours. *Serratia marcescens* is rod-shaped. No obvious precipitate products were observed at 12 hours. At 24 hours, certain granular substances appeared on the cell surface. By the 36th hour, distinct crystalline minerals had formed, exhibiting irregular flaky or lamellar aggregates arranged in a characteristic overlapping or book-like stacking pattern.[32] The aggregates exhibited distinct edges, though their overall margins appeared somewhat irregular due to the layered stacking of constituent crystals.

3.3. Genomic Analysis of *Serratia marcescens*

3.3.1. Strain analysis

Based on comparative analysis of 16S rRNA gene sequences, the screened bacterium exhibited 99.7% similarity to *Serratia marcescens*, indicating a high degree of homology between the two organisms. The phylogenetic tree is presented in Appendix Figure S1. The phylogenetic tree is divided into four major clades, with the screened bacterium clustering with *Serratia marcescens*. This further indicates that the screened bacterium and *Serratia marcescens* are either the same species or very closely related.

In contrast, the screened bacterium shows distant phylogenetic relationships with species from other genera (such as Enterobacter, Klebsiella, etc.), demonstrating their early evolutionary divergence.

Bacterial genome-wide profile information is shown in Appendix Table S2. *Serratia marcescens* harbors one chromosome and four plasmids. Its GC content was 58.93%, which is within the typical range of the close relatives of the genus, and its nucleotide composition is conserved and evolutionarily stable, which is in agreement with the reported results of the study of *Serratia marcescens*;[33] however, it is worth noting that many studies report that the number of plasmids in *Serratia marcescens* ranges from 0 to 1,[34] while the number of plasmids in *Serratia marcescens* (n=4) exceeds this range, which may contribute to adaptation to complex environments, such as tolerance to toxic substances (e.g., antimony). A total of 5224 coding sequences (CDSs) were annotated, indicating a very complex functional repertoire. In addition, 90 tRNAs and 22 rRNAs were identified, also reflecting efficient translation machinery and transcriptional activity.

3.3.2. GO, KEGG, and COG annotation

The results of the GO classification histogram are shown in Figure 3a. In total, 2,673 genes (51.17%) were assigned GO annotations. Genes marked with pink asterisks were prioritized for subsequent protein-protein interaction (PPI) mapping. The same labeling approach was applied to the KEGG and COG annotations.

KEGG functional annotations and pathway enrichment are presented in Figure 3b. In total, 4,097 genes (78.42%) were annotated in KEGG and mapped to 45 pathways across six categories: cellular processes, environmental information processing, genetic information processing, human diseases, metabolism, and organismal systems.

The COG functional annotations of *Serratia marcescens* genes were categorized and counted, and the results are shown in Figure 3c. In total, 4,327 protein-coding genes (82.83%) were assigned to 24 COG categories.

3.3.3. Interaction of Serratia marcescens with antimony

Guided by genome and GO/KEGG/COG annotations, we screened literature-supported genes potentially involved in Sb resistance and transformation. The candidate

genes are listed in Table 1, which includes numerous Sb(III) efflux and antioxidant genes, as well as Sb(V) efflux genes and Sb redox genes.

3.4. Transcriptomics

3.4.1 Transcriptomic validation of Sb resistance and mineralization mechanisms

The transcriptome differential expression volcano plot is shown in Figure 4a. In total, 663 genes were significantly up-regulated and 395 were down-regulated, indicating substantial changes in the transcriptional profile of *Serratia marcescens* under antimony stress. A clustering heatmap of transcriptome expression is presented in Figure 4b, revealing marked differential expression between groups. Figures 4c and 4d show GO enrichment analyses for significantly up-regulated and down-regulated genes, respectively. Similarly, Figures 4e and 4f present the corresponding KEGG enrichment analyses. A clustered heatmap showing up-regulated expression is provided in Appendix Figure S5, down-regulated expression in Appendix Figure S6, and details of differentially expressed genes are included in Appendix Table S3.

The results showed that key functional genes listed in Table 1 were significantly affected by antimony stress. Specifically, Sb(III) efflux genes (*arsA*, *arsB*), Sb(III) chelation gene (*gshA*), anti-oxidative stress genes (*gshA*, *gst*, *soxR*), and Sb(III) oxidation gene (*iscR*) were all significantly up-regulated. In contrast, genes related to Sb(V) uptake (*pstABC*) and catalase genes (*katG*, *katE*) were significantly down-regulated. Additionally, sugar transporters (*malTKXZ*, *glpQK*) were significantly up-regulated. In the metabolic module, amino acid metabolism genes (*ilvB*, *leuABCD*, *argBCDGHR*) were significantly down-regulated, while tricarboxylic acid (TCA) cycle genes (*fumC*, *mdh*) were significantly up-regulated. Fatty acid metabolism genes (*fabAG*) and nucleotide metabolism gene (*nrdD*) were significantly down-regulated. Some outer membrane channel porin genes (*ompCW*) were also significantly down-regulated. The DNA repair module genes (*recANX*, *dnaN*) were significantly up-regulated, and capsular polysaccharide synthesis genes (*rcsA*/*rcsB*) were significantly up-regulated.

3.3.5. Data mining of functional genes

The protein interaction network is shown in Figure 5. Figure 5A, B are key subsets drawn from the upregulated and downregulated genes, respectively. The key information in Figure 5 is summarized in Appendix Table S4.

3.5. Proteomics

3.5.1. Differentially expressed proteins (DEPs)

Quantitative proteomic analysis was performed on the same bacterial samples used for transcriptomics (control vs. 19.47 mM Sb(III)). A total of 3,736 proteins were identified, of which 245 showed significant differential expression, including 143 up-regulated and 102 down-regulated proteins (Figure 6a). Figure 6b presents a proteomic clustering heatmap, revealing marked differences in protein expression among the groups.

3.5.2. GO and KEGG enrichment of DEPs

To elucidate the functional implications of the proteomic changes, GO enrichment analysis was conducted on the 245 differentially expressed proteins (DEPs). The results showed that the DEPs were significantly enriched in categories associated with catalytic activity, transmembrane transport, oxidation-reduction processes, and response to stress (Figure 7a). KEGG pathway enrichment analysis further indicated that the DEPs were significantly enriched in pathways related to siderophore group nonribosomal peptide biosynthesis, the sulfur relay system, and ABC transporters (Figure 7b).

A more detailed examination of the GO annotations revealed that among the DEPs classified under catalytic activity (Figure 7c), the up-regulated proteins were predominantly associated with small molecule binding, hydrolase activity, and oxidoreductase activity, whereas the down-regulated proteins were primarily involved in metabolic processes and organic cyclic compound binding. Regarding transport activity (Figure 7e), the up-regulated DEPs were significantly associated with transmembrane transporter activity and ATPase-coupled transmembrane transport, suggesting an enhanced capacity for substrate translocation and detoxification. For binding activity (Figure 7g), the up-regulated DEPs were enriched in organic cyclic compound binding and small molecule binding, which is consistent with the requirement for enhanced metabolic and regulatory functions under Sb(III) stress.

KEGG enrichment analysis of the up-regulated DEPs (Figure 7d) revealed significant enrichment in pathways crucial for adaptation to Sb(III) stress, including siderophore group nonribosomal peptide biosynthesis, the sulfur relay system, and the bacterial secretion system. In contrast, the down-regulated DEPs (Figure 7f) were significantly enriched in pathways related to bacterial chemotaxis and flagellar assembly, indicating a suppression of motility that may conserve energy for stress defense. Collectively, these proteomic findings align with the transcriptomic results and suggest a coordinated metabolic reprogramming in which cellular resources are redirected toward metal detoxification and defense mechanisms.

3.5.3. Data mining of differential proteins

The key protein-protein interaction (PPI) subnetwork of differentially expressed proteins (DEPs) under Sb(III) stress (Figure 8) reveals that these DEPs form distinct functional clusters, with the upregulated and downregulated proteins exhibiting significantly different interaction patterns.

The upregulated DEP analysis revealed a highly interconnected sub-network centered around the biosynthesis of Fe-S clusters (*SufABCF*, *IcsA*). Iron uptake proteins (*FeoA*, *EfeO*, *EfeB*) and *FhuD* (a ferric carrier binding protein located in the cytoplasmic ring) [35], this protein is coupled with *FbpA* (located in the periplasmic space and binding Fe^{3+})[36] as well as *ExbD* (forming a complex with *ExbB* and *TonB*, using proton motive force to drive the outer membrane receptor) [37]. The key resistance functions provided by *ArsB*, *ArsC*, and *ArsR* are involved. Among them, *ArsR* is considered to be a key regulatory gene that will activate the expression of the *Ars* series in the Sb(III) environment. At the same time, it can also affect the TCA cycle and metal homeostasis-related proteins (such as those regulating iron uptake) [38, 39]. Class Ib ribonucleotide reductase *nrdH*, *nrdF*, and *nrdI* work together to synthesize deoxyribonucleotides (dNTPs), providing raw materials for bacterial DNA replication and repair [40].

In contrast, downregulated DEPs assembled into a distinct subnetwork primarily associated with bacterial motility and chemotaxis (Figure 8b). The inhibition of the expression of glycerol-related proteins (*GlpB*, *GlpC* and *GlpF*) indicates that the bacteria' uptake of glycerol and some alcohols is restricted [41]. Among them, *GlpF* has been

shown to be able to actively transport Sb(III), which further reduces the pathway for Sb(III) to enter the bacteria [42]. The interaction of fumarate reductase iron-sulfur subunit (*FrdB*) and nitrite reductase (*NirD*) within the glycerol-related protein subunits indicates that the three interrelated pathways of anaerobic glycerol decomposition, fumarate respiration, and nitrite reduction are closed [43, 44]. This is a global "anaerobic metabolic shock", aiming to reduce the generation of ROS during the electron transfer process and save the consumption of iron-sulfur clusters. Key components within this subnetwork included the chemotaxis signaling cascade proteins *CheZ* (phosphatase), and flagellar structural elements such as *FliL*, *FliE*, (flagellin) [45, 46]. The expression of citrate metabolism protein (citDEX) and purine ribonucleoside monophosphate biosynthesis (PurDMK) was significantly inhibited [47, 48]. *MiaB* and *RlmN* are two free radical enzymes that function by relying on iron-sulfur clusters. Among them, *MiaB* (methyltransferase) is responsible for modifying tRNA (transfer RNA), while *RlmN* (methyltransferase) is responsible for modifying rRNA (ribosomal RNA) [49]. Their downregulated expression indicates that the bacteria reduce transcription, thereby lowering energy consumption to cope with external stress.

Collectively, PPI network analysis of DEPs corroborates the transcriptomic and GO/KEGG enrichment findings, revealing a coordinated cellular adaptive response to Sb(III) stress characterized by the activation of iron acquisition and cofactor biosynthesis pathways, coupled with the repression of motility and anaerobic metabolism.

4. Discussion

4.1. Energy re-regulation during the mineralization process

One of the most significant metabolic findings of this study is the synergistic upregulation of key enzymes in the tricarboxylic acid (TCA) cycle (*Mqo*, *Mdh*, *FumC*, *IcdA*) and long-chain fatty acid degradation proteins (*FadL*, *FadD*, *FadE*). However, this upregulation is not solely for ATP production. In-depth analysis indicates that under Sb(III) stress, the bacteria face a severe reduction potential (NADH/NADPH) crisis.

On the one hand, once Sb(III) enters the cell, it causes oxidative damage to Fe-S clusters, disrupts the electron transport chain, leads to electron leakage, and induces

ROS; on the other hand, the excretion of Sb(III) by the antimony resistance system (*ArsAB*) is a proton motive force (PMF)-driven active transport process.[50, 51]

To maintain the efficiency of the *ArsB* pump, bacteria must continuously supply NADPH and NADH to the respiratory chain by accelerating fatty acid β-oxidation and the TCA cycle. However, we observed that enzymes associated with anaerobic respiration (such as *FrdB* and *NirD*) were significantly inhibited. This suggests that the bacteria have adopted a strategy that prioritizes aerobic respiration, as aerobic respiration has a higher proton pumping efficiency compared to nitrate or fumarate respiration, enabling the generation of a stronger PFM per unit of substrate consumption.[52] By shutting down inefficient anaerobic energy-generating pathways and fully prioritizing aerobic phosphorylation, the bacteria ensure sufficient energy for Sb(III) efflux and DNA repair.

4.2. Fe-S cluster synthesis and the buffering mechanism against Sb(III) toxicity

Sb(III) exhibits extremely high affinity for thiol groups (-SH) and iron-sulfur clusters in proteins.[53] In this study, the synergistic upregulation of the Fe-S cluster assembly protein (*SufABCS*) and the iron uptake system (*FepA*, *FeoA*, *EfeO*) revealed a metal salvage strategy.

It is worth noting that the Suf system is typically activated during iron deficiency or oxidative stress. In the presence of Sb(III), bacteria perceive not only oxidative stress but also the physical disintegration of iron-sulfur clusters. To repair the dehydrogenases and respiratory chain complexes damaged by Sb(III), bacteria must accelerate the de novo synthesis of new Fe-S clusters. The prerequisite for synthesizing iron-sulfur clusters is an adequate supply of Fe^{2+} and sulfur donors. Therefore, bacteria upregulate iron transporters to seize iron ions from the external environment, while simultaneously significantly upregulating the molybdenum cofactor (*MoaABCDE*). Although Moco is typically associated with nitrogen metabolism and sulfite oxidation, its synthesis involves complex sulfur transfer reactions that consume large amounts of reducing sulfur. This further intensifies the bacteria`s demand for cysteine and sulfides, which explains why sulfur transport systems are highly enriched in proteomic studies—sulfur serves

not only as a raw material for synthesizing glutathione (GSH) but also as a structural element for rebuilding Fe-S clusters and molybdenum cofactors.

It is worth noting that the Suf system is typically activated during iron deficiency or oxidative stress.[54] In the presence of Sb(III), bacteria perceive not only oxidative stress but also the physical disintegration of iron-sulfur clusters. To repair the dehydrogenases and respiratory chain complexes damaged by Sb(III), bacteria must accelerate the de novo synthesis of new Fe-S clusters. The prerequisite for synthesizing iron-sulfur clusters is an adequate supply of Fe^{2+} and sulfur donors. Therefore, bacteria upregulate iron transporters to seize iron ions from the external environment, while simultaneously significantly upregulating the molybdenum cofactor (*MoaABCDE*). Although the molybdenum cofactor is typically associated with nitrogen metabolism and sulfite oxidation, its synthesis involves complex sulfur transfer reactions that consume large amounts of reducing sulfur. This further increases the bacteria demand for cysteine and sulfides, which explains why sulfur transport systems are highly enriched in proteomics studies: sulfur is not only a precursor for the synthesis of glutathione (GSH), but also a structural component in the regeneration of iron-sulfur clusters and molybdenum cofactors.

4.3. The non-classical nucleation pathway of mineralized products: from amorphous precursors to crystalline Sb_2O_3

Time-series analysis using SEM-EDS and Raman spectroscopy (no products at 12 h, particle adhesion at 24 h, appearance of characteristic peaks at 27 h, and complete crystallization at 36 h) provides strong evidence for "non-classical crystallization." Free Sb(III) in solution does not directly overcome the energy barrier to form crystals, but rather undergoes an amorphous precursor stage.

Under acidic conditions (pH 4.67), Sb(III) exists primarily as $Sb(OH)_3$ or as the positively charged SbO^+ ion.[55] The carboxyl (-COOH) and phosphate ($-PO_4$) groups on the bacterial cell wall provide a high density of negatively charged nucleation sites.[56] Initially, these sites rapidly captured Sb(III) through electrostatic adsorption, forming a highly hydrated, structurally disordered gel-like film (the particles observed after 24 hours). Over time,

extracellular polymers (EPS) released through bacterial metabolism, along with changes in the local pH microenvironment, induced dehydration and structural rearrangement of the precursors. Only when the local concentration became supersaturated and the nucleation energy barrier was overcome did the crystalline phase grow from the amorphous matrix. This pathway results in a unique, irregular lamellar (book-like) stacking of Sb_2O_3, which is distinctly different from the isotropic cubic or octahedral Sb_2O_3 morphologies typically observed in purely chemically synthesized samples, thereby providing indirect evidence of the templating role of the bio-organic matrix in regulating crystal orientation and morphology.

4.4. The Underlying Logic of Movement-Induced Inhibition: Energy Conservation and Metal Tolerance

Significant downregulation of flagellar synthesis (*flg* gene cluster) and chemotaxis (*cheR*) suggests that bacteria conserve energy under Sb(III) stress. In-depth metabolic flux analysis reveals that this downregulation serves a dual purpose:

High-Energy-Consuming Function Disabled: A complete rotation of a flagellar motor requires 2.3×10^5 ATP molecules per beat for a flagellum.[57] Halting flagellar synthesis not only conserves amino acid building blocks but, more critically, blocks this channel of massive proton consumption, allowing all protons pumped by the respiratory chain to be directed toward *ArsB*-mediated Sb(III) efflux, thereby raising the antimony resistance threshold (MIC > 250 mM).

Prioritization of LPS/capsule synthesis: We observed upregulation of the capsule polysaccharide synthesis genes (*rcsA*/*rcsB*). After losing motility, the bacteria remodeled their outer membrane structure; the thickened capsule not only served as a physical barrier against antimony ion penetration but also provided a larger specific surface area for the attachment of amorphous minerals, thereby promoting subsequent Sb_2O_3 deposition.

5. Conclusion

This study reports the isolation and characterization of a novel antimony(III)-mineralizing bacterium, Serratia marcescens, from antimony-contaminated slag. This strain exhibits extremely high tolerance to Sb(III) (minimum inhibitory concentration, MIC > 250 mM), achieving 96.18% Sb(III) removal efficiency under conditions optimized by response surface methodology (RSM: 27.7 °C, pH 4.67, 205.6 rpm). Multiple characterization techniques revealed

that the mineralization proceeds via the bacterial formation of amorphous or poorly crystalline minerals, which gradually accumulate on the cell surface and eventually crystallize into Sb_2O_3.

Integrated multi-omics analyses (whole-genome sequencing, transcriptomics, and proteomics) elucidated the molecular response mechanisms underlying this mineralization process:

(1) Accelerated TCA cycle regulates energy metabolism: An energy acquisition mechanism coupling fatty acid uptake and degradation with the TCA cycle is established, while anaerobic respiration and sulfur assimilation pathways are suppressed, thereby enabling more efficient energy production.

(2) Iron uptake and cofactor synergy construct a metal–protein defense line: An iron acquisition pathway coupling siderophore production and iron uptake is established, providing raw materials for molybdenum cofactor synthesis, Fe–S cluster assembly, and glutathione biosynthesis.

(3) Multi-level reactive oxygen species (ROS) scavenging orchestrates antioxidant defense: A comprehensive antioxidant network is assembled, involving catalase, alkyl hydroperoxide reductase, glutathione enzymes, and the *SoxR* sensor protein.

(4) Suppressive regulation shuts down non-essential energy-consuming pathways: Genes encoding flagellar structural proteins, flagellar motor proteins, chemotaxis proteins, and various high-energy-cost amino acid biosynthesis pathways are downregulated.

CRediT authorship contribution statement

Zhiwei Zhou: Data curation; Formal analysis; Investigation; Methodology; Project administration; Software; Validation; Visualization; Writing-original draft; Writing-review & editing. **Peng Zhang:** Conceptualization; Funding acquisition; Resources; Writing-review & editing; Supervision. **Qing Li:** Conceptualization; Resources; Funding acquisition; Supervision; Writing-review & editing. **Xia Hu:** Funding acquisition; Resources; Supervision; Writing-review & editing. **Huan Hu:** Writing-review & editing; Resources. **Aijiang Yang:** Conceptualization; Funding acquisition; Resources; Supervision; review & editing.

Funding sources

This research did not receive any specific grant from funding agencies in the public, commercial, or not-for-profit sectors.

Declaration of Competing Interest

The authors declare that they have no known competing financial interests or personal relationships that could have appeared to influence the work reported in this paper.

Acknowledgements

We sincerely thank Professors Zhang Peng, Yang Aijiang, and Hu Xia for their guidance, financial support, and invaluable resources throughout this experiment. We also extend our gratitude to our fellow graduate students, Hu Huan and Li Qing, for their substantial assistance with experimental design and manuscript writing.

Data availability

Data will be made available on request.

Link to the original raw data of the whole genome and transcriptome: https://www.ncbi.nlm.nih.gov/sra/PRJNA1498215

Link to the original protein data: https://proteomecentral.proteomexchange.org/cgi/GetDataset?ID=PXD081319

References

(1) Smichowski, P. Antimony in the environment as a global pollutant: A review on analytical methodologies for its determination in atmospheric aerosols. *Talanta* **2008** *75* (1), 2-14, Review.

(2) Wysocki, R.; Rodrigues, J. I.; Litwin, I.; Tamas, M. J. Mechanisms of genotoxicity and proteotoxicity induced by the metalloids arsenic and antimony. *Cellular and molecular life sciences : CMLS* **2023** *80* (11), 342-342, ; Review.

(3) Okkenhaug, G.; Zhu, Y.-G.; Luo, L.; Lei, M.; Li, X.; Mulder, J. Distribution, speciation and availability of antimony (Sb) in soils and terrestrial plants from an active Sb mining area. *Environmental Pollution* **2011** *159* (10), 2427-2434.

(4) Bolan, N.; Kumar, M.; Singh, E.; Kumar, A.; Singh, L.; Kumar, S.; Keerthanan, S.; Hoang, S. A.; El-Naggar, A.; Vithanage, M.; et al. Antimony contamination and its risk management in complex environmental settings: A review. *Environment International* **2022** *158*, Review.

(5) Pierart, A.; Shahid, M.; Séjalon-Delmas, N.; Dumat, C. Antimony bioavailability: Knowledge and research perspectives for sustainable agricultures. *Journal of Hazardous Materials* **2015** *289*, 219-234.

(6) Lu, Y. Q.; Wu, J. X.; Li, J. K. The alleviating effects and underlying mechanisms of exogenous selenium on both Sb(III) and Sb(V) toxicity in rice seedlings (Oryza sativa L.). *Environmental Science and Pollution Research* **2023** *30* (38), 89927-89941.

(7) (USGS), U. S. G. S. *USGS Mineral Commodity Summary for 2023: Antimony*; Reston, VA, USA, 2023.

(8) Kanellopoulos, C.; Sboras, S.; Voudouris, P.; Soukis, K.; Moritz, R. Antimony's Significance as a Critical Metal: The Global Perspective and the Greek Deposits. *Minerals* **2024** *14* (2), Review.

(9) Moosavi-Khoonsari, E.; Mostaghel, S.; Siegmund, A.; Cloutier, J.-P. A Review on Pyrometallurgical Extraction of Antimony from Primary Resources: Current Practices and Evolving Processes. *Processes* **2022** *10* (8), Review.

(10) Ashley, P. M.; Craw, D.; Graham, B. P.; Chappell, D. A. Environmental mobility of antimony around mesothermal stibnite deposits, New South Wales, Australia and southern New Zealand. *Journal of Geochemical Exploration* **2003** *77* (1), 1-14.

(11) Ungureanu, G.; Santos, S.; Boaventura, R.; Botelho, C. Arsenic and antimony in water and wastewater: Overview of removal techniques with special reference to latest advances in adsorption. *Journal of Environmental Management* **2015** *151*, 326-342, Review.

(12) Soundari Arockiam Jeyasundar, P. G.; Ali, A.; Azeem, M.; Li, Y.; Guo, D.; Sikdar, A.; Abdelrahman, H.; Kwon, E.; Antoniadis, V.; Mani, V. M.; et al. Green remediation of toxic metals contaminated mining soil using bacterial consortium and Brassica juncea. *Environmental Pollution* **2021** *277*.

(13) Tang, H.; Hassan, M. U.; Nawaz, M.; Yang, W.; Liu, Y.; Yang, B. A review on sources of soil antimony pollution and recent progress on remediation of antimony polluted soils. *Ecotoxicology and Environmental Safety* **2023** *266*, Review.

(14) Zhou, Z.; Yu, H.; Wang, G.; Li, M.; Shi, K. High antimony resistance strain Enterobacter sp. Z1 mediates biomineralization of antimony trioxide. *Environment International* **2025** *195*.

(15) Lai, C.-Y.; Wen, L.-L.; Zhang, Y.; Luo, S.-S.; Wang, Q.-Y.; Luo, Y.-H.; Chen, R.; Yang, X.; Rittmann, B. E.; Zhao, H.-P. Autotrophic antimonate bio-reduction using hydrogen as the electron donor. *Water Research* **2016** *88*, 467-474.
(16) Yamamura, S.; Iida, C.; Kobayashi, Y.; Watanabe, M.; Amachi, S. Production of two morphologically different antimony trioxides by a novel antimonate-reducing bacterium, Geobacter sp. SVR. *Journal of Hazardous Materials* **2021** *411*.
(17) Yang, L.; Yang, A.; Song, L.; Cui, W.; Bian, W.; Niu, A.; Xu, P.; He, S.; Mei, S.; Shi, X. Formation of Sb_2O_3 microcrystals by Rhodotorula mucilaginosa. *Journal of Hazardous Materials* **2024** *469*.
(18) Zhuang, F.; Xiang, X.; Hu, J.; Xiong, J.; Zhang, T.; Zhou, L.; Jiang, G.; Zhang, M.; Liu, Z.; Yin, H.; et al. Behavior and Mechanisms of Antimony Precipitation from Wastewater by Sulfate-Reducing Bacteria Desulfovibrio desulfuricans. *Toxics* **2025** *13* (1).
(19) Xiaohong, N.; Chi-ho, Y.; Dongchu, G.; GouHui; Zhou, J.-X.; Xiawei, P. Biological characteristics of four strains of antimony-tolerant bacteria and their role in promoting growth of oilseed rape in antimony-contaminated soil. *Chinese Journal of Ecology* **2017** *36* (06), 1658-1666. From Cnki.
(20) Zhang, F.; Liu, J.; Jiang, L.; Zheng, Y.; Yu, L.; Du, L. Production of the siderophore lysochelin in rich media through maltose-promoted high-density growth of Lysobacter sp. 3655. *Frontiers in Microbiology* **2024** *15*.
(21) Liu, C.-t.; Hou, H.-g.; Fan, N.-y.; Li, H.-h. Determination of Arsenic, Antimony, Mercury and Selenium in Different Parts of Acanthopanax Senticosus Harms by Atomic Fluorescence Spectrometry. *Spectroscopy and Spectral Analysis* **2010** *30* (4), 1123-1125.
(22) Gutierrez Rodriguez, E. K.; Astudillo-Melgar, F.; Larios, V.; Bolivar, F.; Escalante, A.; Giles-Gomez, M. The complete genome of two Lactiplantibacillus plantarumisolates from the traditional Mexican fermented pulque beverage assembled with a combination of PacBio and Illumina platforms. *Microbiology resource announcements* **2024** *13* (1), e0098523-e0098523.
(23) Liu, Z.; Xiao, Z.; Geng, R.; Ren, M.; Wu, X.; Xie, H.; Bai, G.; Zhang, H.; Liu, D.; Jiang, C.; et al. Transcriptome Analysis and Genome-Wide Gene Family Identification Enhance Insights into Bacterial Wilt Resistance in Tobacco. *Agronomy-Basel* **2024** *14* (2).
(24) Nigiz, S.; Kulabas, N.; Ture, A.; Kablan, S. E.; Kocak, E.; Ozkul, C.; Hazirolan, G.; Nemutlu, E.; Kucukguzel, I. Comprehensive Proteomic and Metabolomic Analysis of Novel Substituted Fluoroquinolone Derivatives in *Escherichia coli* Isolates. *Biomedical chromatography : BMC* **2026** *40* (4), e70407-e70407.
(25) Hussein, S. A.; Taha, G. M.; Adam, F. A.; Moghazy, M. A. Three different methods for ZnO-RGO nanocomposite synthesis and its adsorption capacity for methylene blue dye removal in a comparative study. *Bmc Chemistry* **2025** *19* (1).
(26) Fang, D.; He, F.; Xie, J.; Xue, L. Calibration of Binding Energy Positions with C1s for XPS Results. *Journal of Wuhan University of Technology-Materials Science Edition* **2020** *35* (4), 711-718.
(27) Zanna, S.; Mercier, D.; Gardin, E.; Allion-Maurer, A.; Marcus, P. EPS for bacterial anti-adhesive properties investigated on a model metal surface. *Colloids and Surfaces B-Biointerfaces* **2022** *213*.
(28) J.F. Moulder, W. F. S., P.E. Sobol, K.D. Bomben, J. Chastain. Handbook of X-ray Photoelectron Spectroscopy. **1992**.

(29) Linarez Perez, O. E.; Sanchez, M. D.; Lopez Teijelo, M. Characterization of growth of anodic antimony oxide films by ellipsometry and XPS. *Journal of Electroanalytical Chemistry* **2010** *645* (2), 143-148.
(30) Freitas, M. B. J. G.; Eiras, C.; Bulhões, L. O. S. Breakdown of the niobium oxide film under galvanostatic polarisation and in acid solutions. *Corrosion Science* **2004** *46* (5), 1051-1060.
(31) Li, X. Y.; Akiyama, E.; Habazaki, H.; Kawashima, A.; Asami, K.; Hashimoto, K. An XPS study of passive films on sputter-deposited Cr-Nb alloys in 12 M HCl solution. *Corrosion Science* **1998** *40* (4), 821-838.
(32) Dey, C.; Das, R.; Poddar, P.; Banerjee, R. Solid Phase Morphological Diversity of a Rare Vanadium Cubane (V_4O_{16}) Based Metal Organic Framework. *Crystal Growth & Design* **2012** *12* (1), 12-17.
(33) Valiatti, T. B.; Bessa-Neto, F. O.; Santos, F. F.; Silva, R. G. B.; Veiga, R.; Cassu-Corsi, D.; Moura, T. C. F.; Lobato, A. R. F.; Pignatari, A. C. C.; Souza, C. O.; et al. Clonal dissemination of highly virulent Serratia marcescens strains producing KPC-2 in food-producing animals. *One Health* **2023** *17*.
(34) Ramdass, A. C.; Rampersad, S. N. Genome-resolved analysis of Serratia marcescens strain SMTT infers niche specialization as a hydrocarbon-degrader. *DNA Research* **2025** *32* (1).
(35) Bharti, S.; Carlini, L.; Esposito, A.; Benini, S. Bioinformatics and modelling studies of FhuD, the periplasmic siderophore binding protein from the plant pathogen *Erwinia amylovora*. *Plos One* **2025** *20* (7).
(36) Ducos, K.; Hakil, F.; Yin, N. H.; Kinska, K.; Angaits, A.; Celis, F. C.; Lobinski, R.; Nolivos, S.; Grimaud, R. Siderophore-Dependent and -Independent Iron Acquisition Pathways in Marinobacter Nauticus SP17. *Environmental Microbiology* **2025** *27* (9).
(37) Zinke, M.; Lejeune, M.; Mechaly, A.; Bardiaux, B.; Boneca, I. G.; Delepelaire, P.; Izadi-Pruneyre, N. Ton motor conformational switch and peptidoglycan role in bacterial nutrient uptake. *Nature Communications* **2024** *15* (1).
(38) Larson, J.; Sather, B.; Wang, L.; Westrum, J.; Tokmina-Lukaszewska, M.; Pauley, J.; Copie, V.; McDermott, T. R.; Bothner, B. Metalloproteomics Reveals Multi-Level Stress Response in *Escherichia coli* When Exposed to Arsenite. *International Journal of Molecular Sciences* **2024** *25* (17).
(39) Chen, X.; Yao, H.; Song, D.; Lin, J.; Zhou, H.; Yuan, W.; Song, P.; Sun, G.; Xu, M. A novel antimony-selective ArsR transcriptional repressor and its specific detection of antimony trioxide in environmental samples via bacterial biosensor. *Biosensors & Bioelectronics* **2023** *220*.
(40) Crona, M.; Torrents, E.; Rohr, A. K.; Hofer, A.; Furrer, E.; Tomter, A. B.; Andersson, K. K.; Sahlin, M.; Sjoberg, B.-M. NrdH-Redoxin Protein Mediates High Enzyme Activity in Manganese-reconstituted Ribonucleotide Reductase from *Bacillus anthracis*. *Journal of Biological Chemistry* **2011** *286* (38), 33053-33060.
(41) Nummela, L.; Lyra, C.; Pitkanen, L.; Maina, H. N.; Makela, M. R. Characterization of three glycerol transporters with broad sugar specificities from Aspergillus niger. *Applied microbiology and biotechnology* **2026**.
(42) Raturi, G.; Sharma, Y.; Mandlik, R.; Kumawat, S.; Rana, N.; Dhar, H.; Tripathi, D. K.; Sonah, H.; Sharma, T. R.; Deshmukh, R. Genomic Landscape Highlights Molecular

Mechanisms Involved in Silicate Solubilization, Stress Tolerance, and Potential Growth-Promoting Activity of Bacterium *Enterobacter* sp. LR6. *Cells* **2022** *11* (22).
(43) Tong, C. Y.; Tomita, H.; Miyazaki, K.; Derek, C. J. C.; Honda, K. KEIO knockout collection reveals metabolomic crosstalk in *Chlorella* spp.-*Escherichia coli* co-cultures. *Journal of Phycology* **2025** *61* (3), 443-462.
(44) Izumi, A.; Schnell, R.; Schneider, G. Crystal structure of NirD, the small subunit of the nitrite reductase NirbD from *Mycobacterium tuberculosis* at 2.0 Å resolution. *Proteins-Structure Function and Bioinformatics* **2012** *80* (12), 2799-2803.
(45) Xu, X.; Li, H.; Qi, X.; Chen, Y.; Qin, Y.; Zheng, J.; Jiang, X. *cheA*, *cheB*, *cheR*, *cheV*, and *cheY* Are Involved in Regulating the Adhesion of *Vibrio harveyi*. *Frontiers in Cellular and Infection Microbiology* **2021** *10*.
(46) Jyot, J.; Dasgupta, N.; Ramphal, R. *FleQ*, the major flagellar gene regulator in Pseudomonas aeruginosa, binds to enhancer sites located either upstream or atypically downstream of the RpoN binding site. *Journal of bacteriology* **2002** *184* (19), 5251-5260, ; Research Support, U.S. Gov't, P.H.S.
(47) Gu, Y.; Huang, L.; Wu, C.; Huang, J.; Hao, H.; Yuan, Z.; Cheng, G. The Evolution of Fluoroquinolone Resistance in *Salmonella* under Exposure to Sub-Inhibitory Concentration of Enrofloxacin. *International Journal of Molecular Sciences* **2021** *22* (22).
(48) Martin, M. G.; Sender, P. D.; Peiru, S.; de Mendoza, D.; Magni, C. Acid-inducible transcription of the operon encoding the citrate lyase complex of Lactococcus lactis Biovar diacetylactis CRL264. *Journal of bacteriology* **2004** *186* (17), 5649-5660, ; Research Support, Non-U.S. Gov't.
(49) McCarthy, E. L. Destruction and Reformation of an Iron-Sulfur Cluster during Catalysis by Lipoyl Synthase. Dissertation/Thesis, 2020. <Go to ISI>://PQDT:68430009.
(50) Liu, H.; Zhuang, W.; Zhang, S.; Rensing, C.; Huang, J.; Li, J.; Wang, G. Global Regulator IscR Positively Contributes to Antimonite Resistance and Oxidation in *Comamonas testosteroni* S44. *Frontiers in Molecular Biosciences* **2015** *2*.
(51) Meng, Y.-L.; Liu, Z.; Rosen, B. P. As(III) and Sb(III) uptake by GlpF and efflux by ArsB in Escherichia coli. *The Journal of biological chemistry* **2004** *279* (18), 18334-18341, ; Research Support, U.S. Gov't, P.H.S.
(52) Kalnenieks, U.; Balodite, E.; Rutkis, R. Metabolic Engineering of Bacterial Respiration: High vs. Low P/O and the Case of *Zymomonas mobilis*. *Frontiers in Bioengineering and Biotechnology* **2019** *7*, Review.
(53) Han, Y.; Liu, B.; Yin, Z.; Shan, X.; Zhang, M.; Jing, C.; Jiang, W. Sb(V) has distinct cellular uptake route and cytotoxic mechanism from Sb (III): Anion channel 2 and sulfhydryl binding. *Journal of Hazardous Materials* **2025** *495*.
(54) Pieper, R.; Huang, S.-T.; Parmar, P. P.; Clark, D. J.; Alami, H.; Fleischmann, R. D.; Perry, R. D.; Peterson, S. N. Proteomic analysis of iron acquisition, metabolic and regulatory responses of *Yersinia pestis* to iron starvation. *Bmc Microbiology* **2010** *10*.
(55) Sun, X.; Li, Y.; Liu, C.; Zhang, L.; Li, Z.; Hao, C. Morphological Distribution and Formation Mechanisms of Antimony in the Shallow Groundwater of the Xikuangshan Antimony Mine in Hunan, China. *Frontiers in Environmental Science* **2022** *10*.
(56) Mishra, S.; Dubey, P.; Naseem, M.; Rishi, S.; Patel, A.; Srivastava, P. K. A kinetic modelling approach to explore mechanism of Cr(VI) detoxification by a novel strain

Pseudochrobactrum saccharolyticum NBRI-CRB 13 using response surface methodology. *World Journal of Microbiology & Biotechnology* **2024** *40* (10).
(57) Chen, D. T. N.; Heymann, M.; Fraden, S.; Nicastro, D.; Dogic, Z. ATP Consumption of Eukaryotic Flagella Measured at a Single-Cell Level. *Biophysical Journal* **2015** *109* (12), 2562-2573.
(58) Zhou, T.; Radaev, S.; Rosen, B. P.; Gatti, D. L. Structure of the ArsA ATPase: the catalytic subunit of a heavy metal resistance pump. *The EMBO journal* **2000** *19* (17), 4838-4845, ; Research Support, U.S. Gov't, P.H.S.
(59) Deng, R.; Chen, Y.; Deng, X.; Huang, Z.; Zhou, S.; Ren, B.; Jin, G.; Hursthouse, A. A Critical Review of Resistance and Oxidation Mechanisms of Sb-Oxidizing Bacteria for the Bioremediation of Sb(III) Pollution. *Frontiers in Microbiology* **2021** *12*, Review.
(60) Yang, R.; Viswanatham, T.; Huang, S.; Li, Y.; Yu, Y.; Zhang, J.; Chen, J.; Herzberg, M.; Feng, R.; Rensing, C. A Sb(III)-specific efflux transporter from Ensifer adhaerens E-60. *Microbiological Research* **2024** *286*.
(61) Roy, U.; Barber, P.; Tse-Dinh, Y.-C.; Batrakova, E. V.; Mondal, D.; Nair, M. Role of MRP transporters in regulating antimicrobial drug inefficacy and oxidative stress-induced pathogenesis during HIV-1 and TB infections. *Frontiers in Microbiology* **2015** *6*, Review.
(62) Gu, J.; Yao, J.; Duran, R.; Sunahara, G. Comprehensive genomic and proteomic profiling reveal Acinetobacter johnsonii JH7 responses to Sb(III) toxicity. *Science of the Total Environment* **2020** *748*.
(63) Uhlich, G. A. KatP contributes to OxyR-regulated hydrogen peroxide resistance in Escherichia coli serotype O157:H7. *Microbiology-Sgm* **2009** *155*, 3589-3598.
(64) Lu, J.; Yang, F.; Li, Y.; Zhang, X.; Xia, B.; Jin, C. Reversible conformational switch revealed by the redox structures of Bacillus subtilis thiol peroxidase. *Biochemical and Biophysical Research Communications* **2008** *373* (3), 414-418.
(65) Wongsaroj, L.; Saninjuk, K.; Romsang, A.; Duang-nkern, J.; Trinachartvanit, W.; Vattanaviboon, P.; Mongkolsuk, S. Pseudomonas aeruginosa glutathione biosynthesis genes play multiple roles in stress protection, bacterial virulence and biofilm formation. *Plos One* **2018** *13* (10).
(66) Kanai, T.; Takahashi, K.; Inoue, H. Three distinct-type glutathione S-transferases from Escherichia coli important for defense against oxidative stress. *Journal of biochemistry* **2006** *140* (5), 703-711.
(67) Anes, J.; Dever, K.; Eshwar, A.; Nguyen, S.; Cao, Y.; Sivasankaran, S. K.; Sakalauskaite, S.; Lehner, A.; Devineau, S.; Daugelavicius, R.; et al. Analysis of the Oxidative Stress Regulon Identifies *soxS* as a Genetic Target for Resistance Reversal in Multidrug-Resistant *Klebsiella pneumoniae*. *Mbio* **2021** *12* (3).
(68) Yamamoto, Y.; Kamio, Y.; Higuchi, M. Cloning, nucleotide sequence, and disruption of Streptococcus mutans glutathione reductase gene (gor). *Bioscience, biotechnology, and biochemistry* **1999** *63* (6), 1056-1062, ; Research Support, Non-U.S. Gov't.
(69) Pan, Y.; Deng, R.; Jin, C.; Li, Y.; Ren, B.; Hou, B.; Wang, C.; Yang, X.; Hursthouse, A. Isolation and Identification of Highly Sb-Resistant Rhodotorula glutinis Strain J5 and its Mechanism of Resistance to Sb(III). *Current Microbiology* **2024** *81* (10), Review.

(70) Xiao, S.; Wang, W.; Amanze, C.; Anaman, R.; Fosua, B. A.; Zeng, W. Antimony oxidation and whole genome sequencing of Phytobacter sp. X4 isolated from contaminated soil near a flotation site. *Journal of Hazardous Materials* **2023** *445*.

749 Table 1. Summary of *Serratia marcescens* functional genes associated with anti-

750 mony resistance/transformation

Category	Gene	Function
Sb(III) transport	*arsA*[58, 59], *arsB*[58, 59], *antB*[60], *mrp*[61]	Efflux of Sb(III) from cells
	not found	Uptake of Sb(III)
Sb(V) transport	not found	Exclusion of Sb(V) from cells
	pstS[62], *pstA*[62], *pstB*[62], *pstC*[62]	Uptake of Sb(V) from outside
anti-oxidative stress	*katG*[63], *katE*[63], *ahpC*[63], *tpx*[64], *gshA*[65], *gshB*[65], *gst*[66], *soxR*[67], *soxS*[67], *oxyR*[67], *gor*[68], *sod*[69]	Degradation of excessive ROS
redox of anti-mony	*arsC*[59]	Reduction of Sb(V) to Sb(III)
	iscR[70], *arsH*[70]	Oxidation of Sb(III) to Sb(V)

751

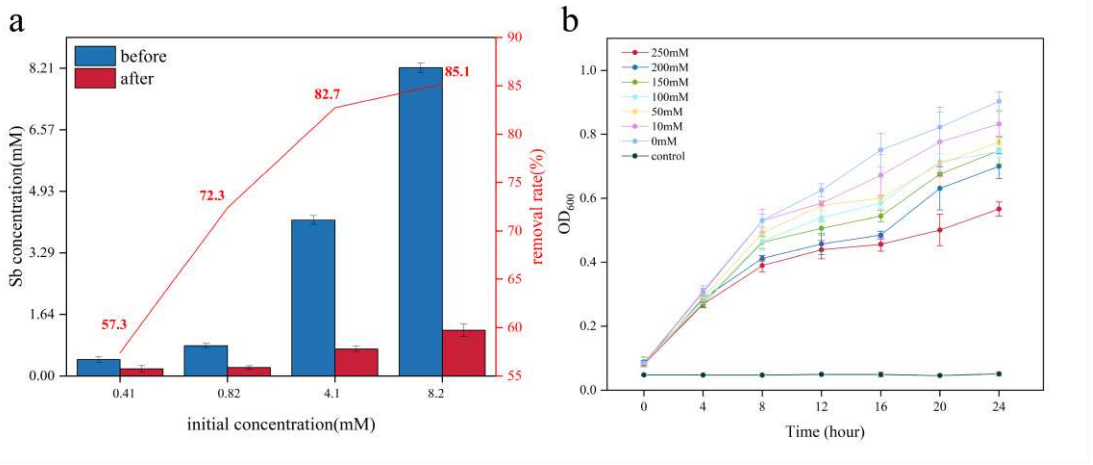


Figure 1. (a) 5-day removal of antimony by *Serratia marcescens* at different Sb concentrations; (b) the minimum inhibitory concentration (MIC) of Sb(III) for the strain

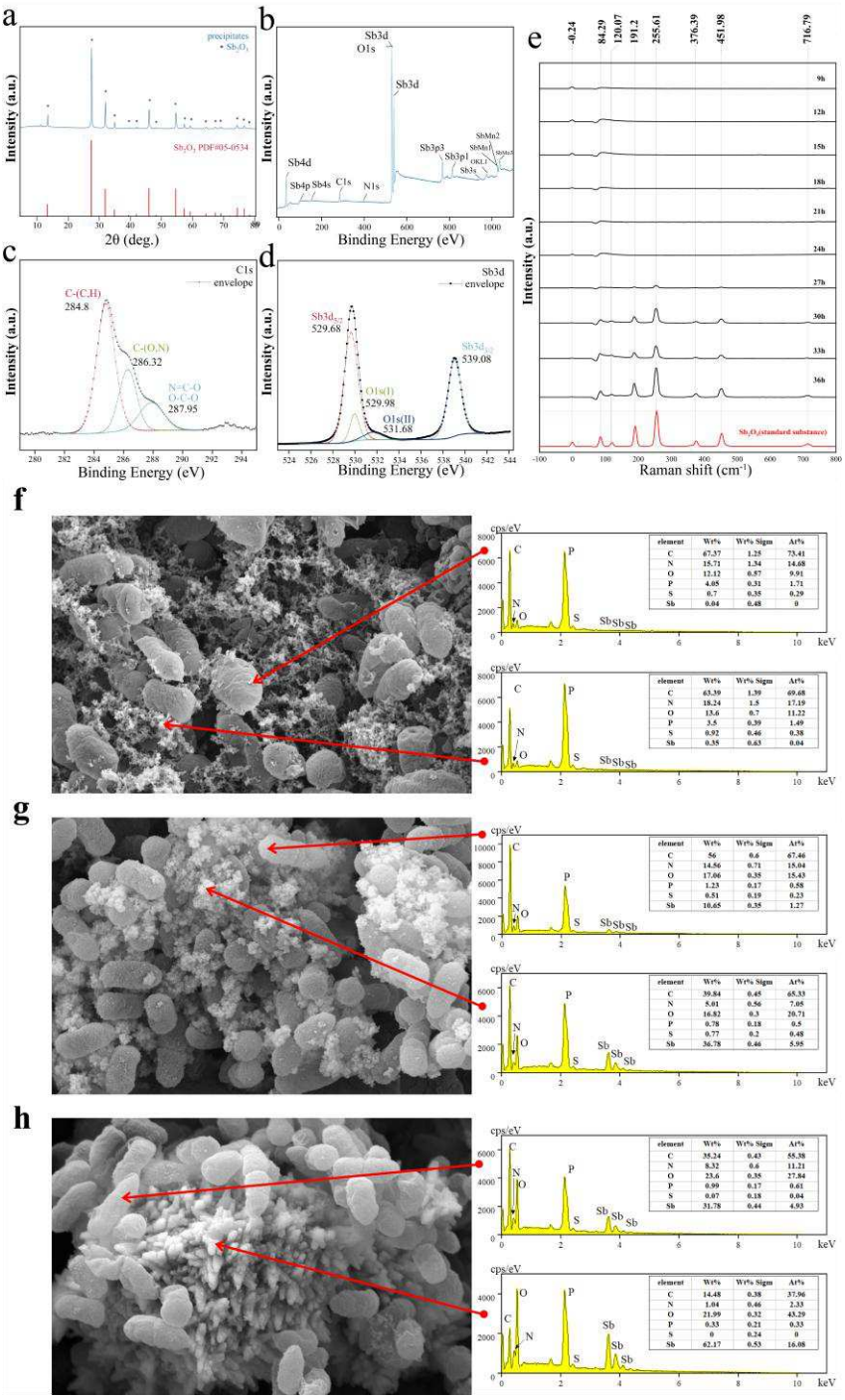


Figure 2. (a) The XRD spectral peaks of the precipitated products; (b) The full spectrum of the precipitate product XPS; (c) The fine spectrum of the C1s orbital of the precipitated product XPS; (d) The fine spectrum of the Sb3d orbital of the precipitated product XPS; (e) Time-dependent Raman characterization results; (f), (g), and (h) are the SEM-EDS characterization results of bacteria at 12, 24, and 36 hours, respectively.

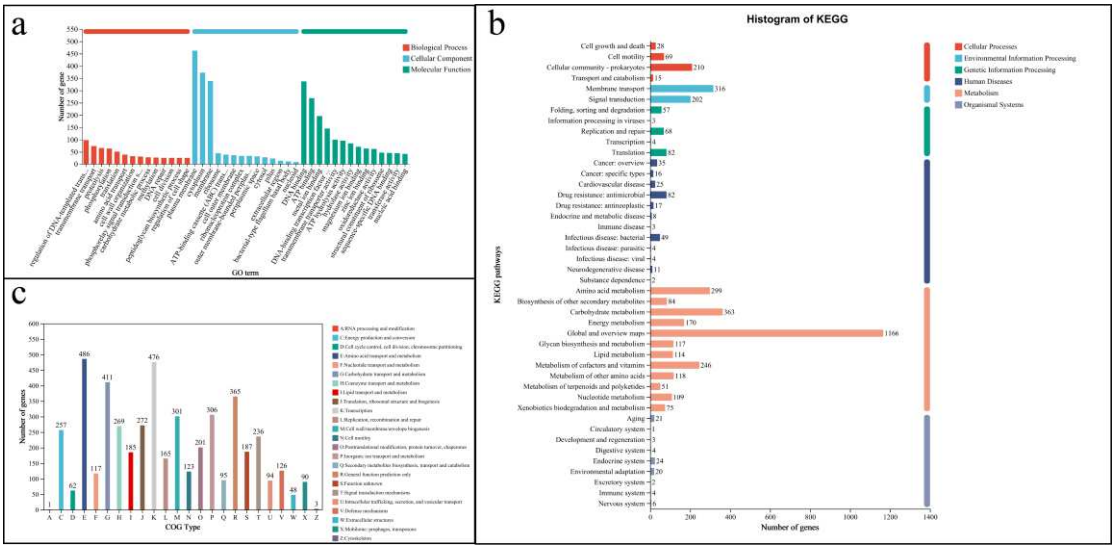


Figure 3. (a) GO Classification Statistics, (b) Pathway classification statistics, (c) COG annotation classification statistics

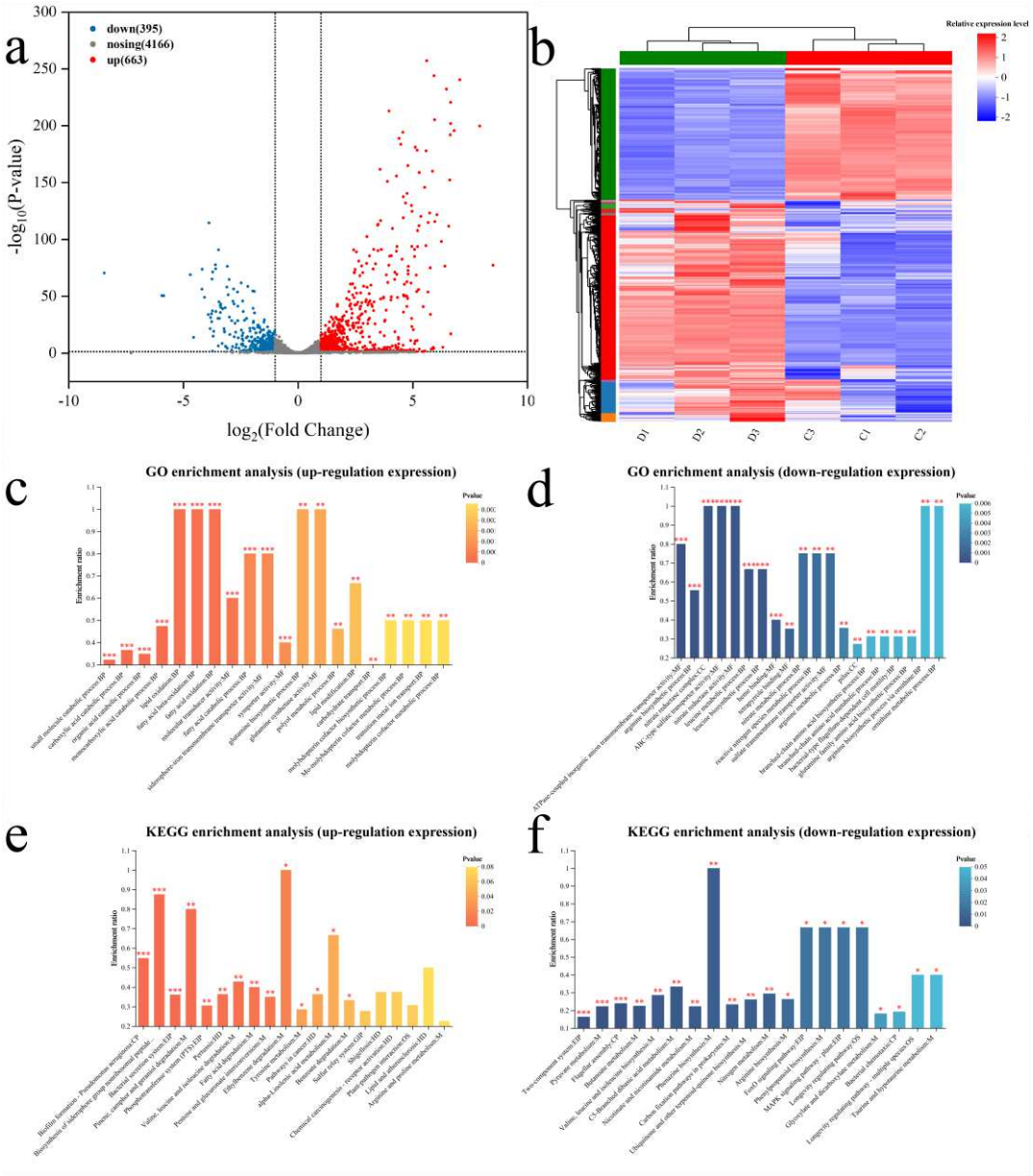


Figure 4. (a) Expression difference volcano plot, Red indicates up-regulated expression, blue indicates down-regulated expression, (b) cluster analysis chart, (c) and (d) GO enrichment analyses of significantly up-expressed and significantly down-expressed genes, respectively, (e) and (f) KEGG enrichment analyses of significantly up-regulated and significantly down-regulated expressed genes, respectively, P-value<0.001 is labelled as ***, P-value<0.01 is labelled as **, P-value<0.05 is labelled as * .

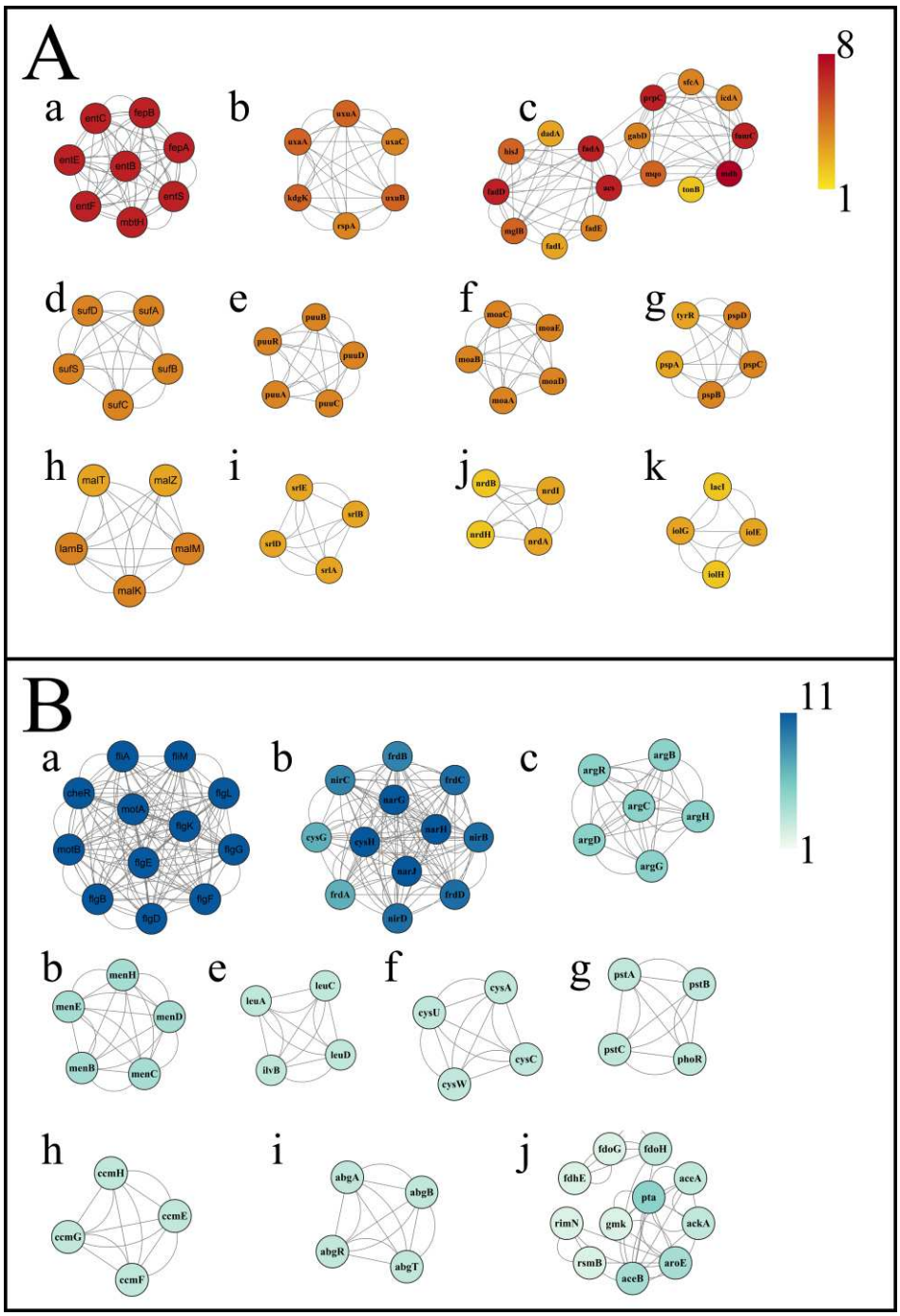
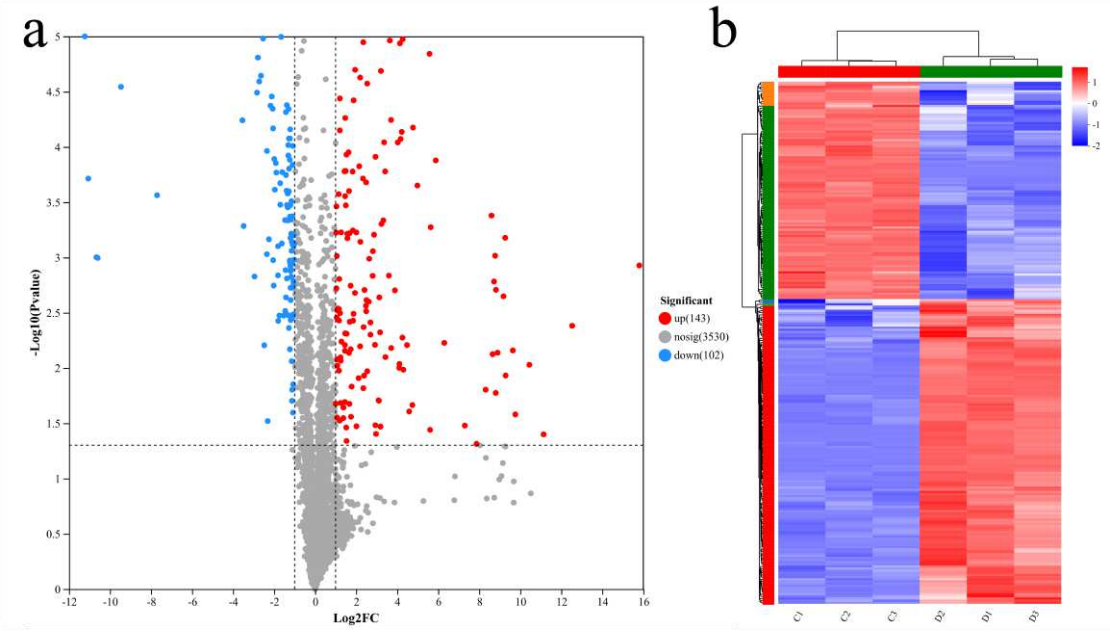


Figure 5. Protein interaction network based on a subset of key genes



781

782 Figure 6. (a) Volcano plot of differentially expressed proteins, (b) proteome clustering

783 heatmap

784

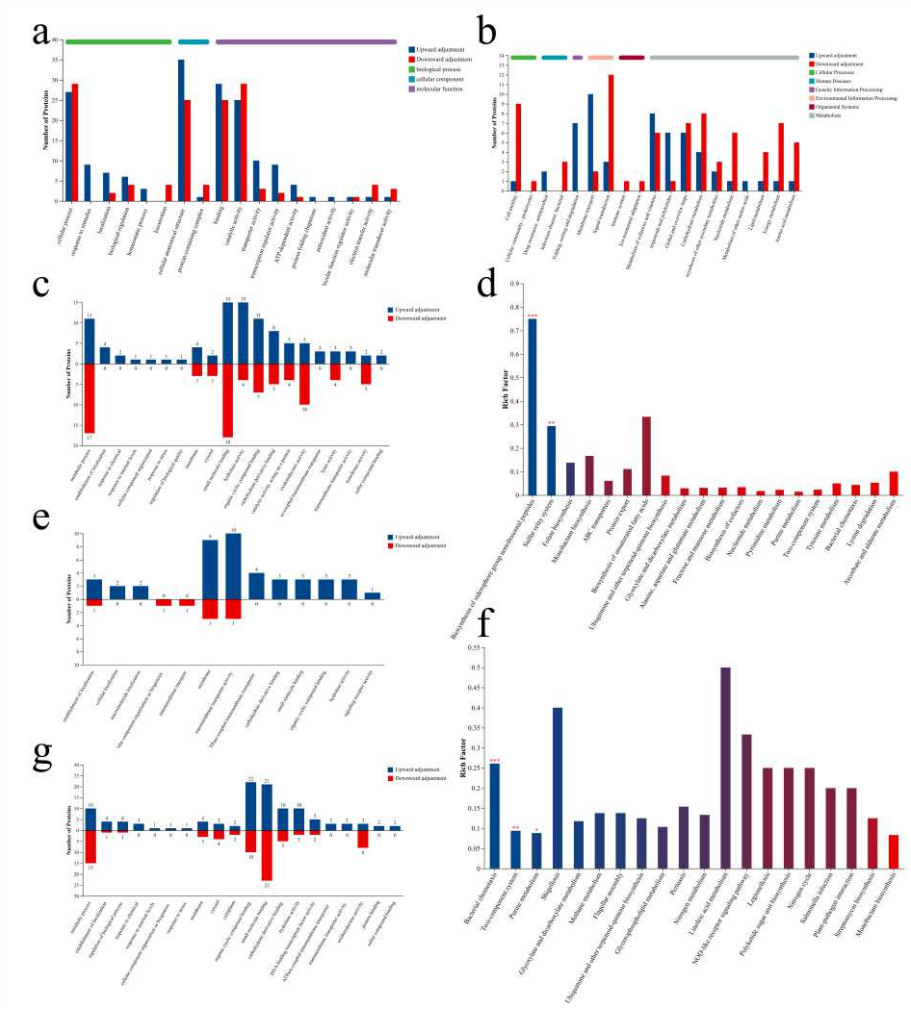


Figure 7. (a)GO functional annotation of differentially expressed proteins in S. marcescens ZG after Sb（III） stress, (b) KEGG functional annotation of differentially expressed proteins in S. marcescens ZG after Sb(III) stress, (c) Statistical analysis of the third-level GO annotations of DEPs with catalytic activity, (e) Statistical analysis of the third-level GO annotations of DEPs with transport activity, (g) Statistical analysis of the third-level GO annotations of DEPs with bonding activity, KEGG enrichment analysis of the up-regulated (d) and down-regulated (f) proteins of S. marcescens ZG after Sb(III) stress. The color of the columns in the figure becomes more blue, indicating a more significant enrichment of the pathway. The abscissa represents the KEGG pathway name, and the ordinate represents the enrichment rate, which is the ratio of the number of proteins enriched to the total annotated proteins of the pathway. The larger the value, the higher the enrichment degree. Those with $P < 0.001$ are marked with ***, those with $P < 0.01$ are marked with **, and those with $P < 0.05$ are marked with *.

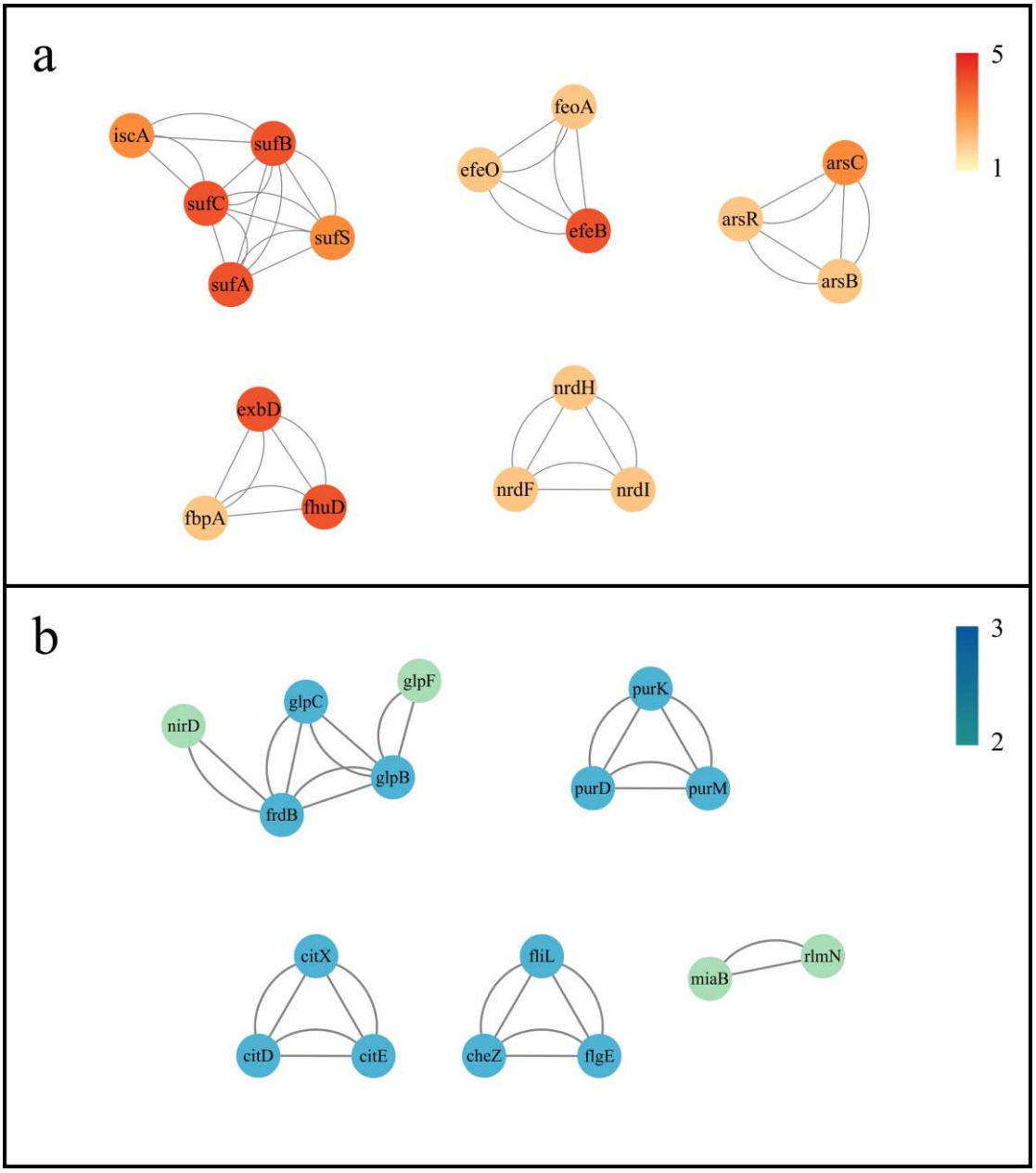


Figure 8. (a) and down-regulated (b) DEPs. The darker the color and the larger the shape, the closer the interaction between the proteins is. In the key subgraphs, the proteins with the prefix "CDG" are the names in the STRING database, but there is no experimental data indicating the predicted functions of these proteins.

Supplementary Files

This is a list of supplementary files associated with this preprint. Click to download.

- AppendixTableS1.docx
- AppendixTableS2.docx
- AppendixTableS4.docx
- AppendixTableS3.csv
- AppendixFigureS4.png
- AppendixFigureS1.png
- AppendixFigureS2.png
- AppendixFigureS6.png
- AppendixFigureS5.png
- AppendixFigureS3.png